

Original citation:

Hosseinzadeh, Elham, Marco, James and Jennings, Paul A. (2018) The impact of multi-layered porosity distribution on the performance of a lithium ion battery. Applied Mathematical Modelling, 61 . pp. 107-123. doi:10.1016/j.apm.2018.04.001

Permanent WRAP URL:

<http://wrap.warwick.ac.uk/101743>

Copyright and reuse:

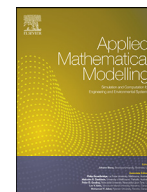
The Warwick Research Archive Portal (WRAP) makes this work of researchers of the University of Warwick available open access under the following conditions.

This article is made available under the Creative Commons Attribution 4.0 International license (CC BY 4.0) and may be reused according to the conditions of the license. For more details see: <http://creativecommons.org/licenses/by/4.0/>

A note on versions:

The version presented in WRAP is the published version, or, version of record, and may be cited as it appears here.

For more information, please contact the WRAP Team at: wrap@warwick.ac.uk



The impact of multi-layered porosity distribution on the performance of a lithium ion battery

Elham Hosseinzadeh*, James Marco, Paul Jennings

WMG, University of Warwick, Coventry CV4 7AL, United Kingdom

ARTICLE INFO

Article history:

Received 12 October 2017

Revised 26 March 2018

Accepted 5 April 2018

Available online 18 April 2018

Keywords:

Multi-layered porosity

Lithium ion battery

3D modelling

Numerical modelling

ABSTRACT

This study investigates the impact of a multi-layered porosity profile on the electrical and thermal performance of a lithium-ion battery. Consideration is given to key attributes of the battery, namely its specific power and energy and the temperature distribution that may generated throughout the cell under electrical load. The COMSOL Multiphysics software tool has been employed to develop a 3D electrochemical-thermal model of a commercially available 10 Ah lithium iron phosphate cell. Through an extensive simulation study, for a fixed value of active material, the impact of varying the porosity profile across both the thickness and height of the electrode has been studied. For each case study, the distribution of reaction current and the corresponding localised state of charge and temperature profile are quantified for a constant current discharge of 5C. Simulation results highlight that a multi-layered porosity distribution across the thickness of the electrode has the potential to yield superior battery performance compared to when the porosity is varied along the electrode height. Moreover, the total heat generation within the cathode may be reduced by up to 14% compared to a Reference Case, along with 0.33% and 0.44% improvement in the specific energy and power, respectively.

© 2018 The Authors. Published by Elsevier Inc.

This is an open access article under the CC BY license.

(<http://creativecommons.org/licenses/by/4.0/>)

1. Introduction

A number of recent studies have highlighted that lithium ion batteries have become the dominant battery technology for many automotive and transport applications. One of the primary reasons for their adoption is their relatively high energy density and high power density (both gravimetric and volumetric) compared to alternative battery technologies. However, it is well understood that there is an inherent trade-off that must be optimised, when designing a new cell to achieve the energy and power targets expressed by a number of vehicle manufacturers and national research bodies. Recent studies, through both numerical simulation and experimental evaluation, have attempted to quantify the trade-off for different cell chemistries and manufacturing processes. The underpinning trend in the results presented is that increasing the power density is only possible at the cost of reduced energy density [1]. Power density can be improved either by replacing a portion of the active material with conductive fillers and through using large pores for ion transport or through the use of thinner electrodes. Both approaches to cell design and manufacture result in lower values of active material within the cell that consequently lead to a reduction in energy density [1,2].

* Corresponding author.

E-mail address: e.hosseinzadeh@warwick.ac.uk (E. Hosseinzadeh).

Nomenclature

List of symbols

$brugg_n$	Bruggeman constant
C	Li^+ concentration (mol m^{-3})
C_p	heat capacity ($\text{J (kg K}^{-1}\text{))}$)
D	diffusion coefficient ($\text{m}^2 \text{s}^{-1}$)
E_{cell}	specific energy (W h kg^{-1})
H	cell height (m)
I	current load (A)
i	current density (A m^{-2})
i_e	ionic current density (A m^{-2})
i_s	electronic current density (A m^{-2})
K	thermal conductivity (W (mK)^{-1})
k	reaction rate (m s^{-1})
L	thickness of the electrode (μm)
m_{cell}	total weight of the cell (kg)
m_s	weight of the active material (kg)
n_p	number of particles in the electrode
P_{cell}	specific power (W/kg)
Q	heat generation (W)
$Q_{ohmic,e}$	electronic ohmic heat (W)
$Q_{ohmic,i}$	ionic ohmic heat (W)
R	universal gas constant ($\text{J mol}^{-1} \text{K}^{-1}$)
r_p	particle radius (μm)
T	temperature ($^{\circ}\text{C}$)
t_{dis}	discharge time (s)
V_t	terminal voltage (V)
x	local SOC of the anode
y	local SOC of the cathode

Greek letters

ε	volume fraction
k_D^{eff}	diffusional conductivity
ρ	density (kg m^{-3})
σ	electronic conductivity (S m^{-1})
κ	ionic conductivity (S m^{-1})
τ	tortuosity
ϕ	thermal properties
φ	potential

Subscripts/superscripts

act	activation
ave	average
e	electrolyte
eff	effective
neg	negative
pos	positive
ref	reference
rev	reversible
s	solid

Terms and abbreviation

sim	simulation
exp	experimental

A consensus does not yet exist as to the optimal design of battery cell, in terms of both chemistry and form-factor. There is significant research characterizing the different chemistries, including: lithium cobalt oxide (LiCoO_2), lithium iron phosphate oxide (LiFePO_4), lithium nickel cobalt manganese ($\text{NCM-LiNi}_x\text{Co}_y\text{Mn}_x\text{O}_z$) and lithium titanate oxide ($\text{LTO-Li}_4\text{Ti}_5\text{O}_{12}$). The battery performance that can be achieved is guided by the choice of material, the design of the

battery, its internal resistance, the electrode properties and the voltage limit for the side reactions [2]. Narrowing the gap between the theoretical and actual useable capacity is a key requirement for improving battery performance [3]. Several research studies have been published that employ novel optimisation approaches to improve the design of high performance batteries [4–6]. Miranda et al. [4] performed geometry optimisation of a lithium ion battery using the finite element method of simulation. Their research took into account different geometries, including conventional and unconventional shapes such as horseshoe, spiral, ring, antenna and gear batteries. Mitchell and Ortiz [5] applied computational topology optimisation methods in an attempt to improve the performance of lithium ion batteries that employ a silicon anode. They addressed the structural and conduction design criteria to concurrently minimise the volume expansion of the anode and to maximise its electronic conductivity. A similar study is reported by Ji et al. [6] in which key material properties within the cell are optimised to improve the low temperature performance of the cell, namely increasing the energy capacity of the cell under a 1C discharge at a temperature of -20°C .

Irrespective of the exact choice of battery chemistry, there are important design parameters which can be varied within the manufacturing process to improve cell performance. These include electrode thickness, particle size, porosity, electrode surface area, geometry and the dimensions of the current collectors [7]. Newman and co-workers [8–10] applied new mathematical approaches to optimise the design variables of a lithium ion battery. They developed a simplified battery model to facilitate the mathematical formulation of the problem and to allow the optimisation of the porosity and electrode thickness [8]. Discharge time and cell capacity were found to be the most significant factors affecting their final design. Further, they also investigated the influence of different particle size distributions on the operation of porous electrodes [9]. Their research continued as they developed a full cell model to evaluate the ohmic related energy loss of the solid electrolyte interface (SEI) layer. Their model was used to optimise the design of a graphite–iron phosphate cell [10]. In addition, the authors continued to develop a comparable model to optimise and evaluate the performances of both graphite and titanate negative electrodes [11].

Other researchers have employed higher fidelity models and carried out parametric studies to quantify the impact of specific design variables on cell heat generation [12] and the electrical performance of a lithium ion battery [13]. Wu et al. [12] developed a coupled electrochemical–thermal model to evaluate the impact of particle size and electrode thickness on battery performance and heat generation rate. Du et al. [13] introduced a new surrogate modelling framework to map the effect of design parameters, such as cathode particle size, diffusion coefficient and electronic conductivity on battery performance in terms of specific energy and power. They quantified the relative impact of various parameters through a global sensitivity analysis using a cell-level model in conjunction with methods such as kriging, polynomial response, and radial-basis neural network. In addition to these numerical works, Singh et al. [14] investigated experimentally the amount of energy that may be extracted from a cell manufactured using thick electrodes ($320\mu\text{m}$) compared to cells that employ a thinner electrode ($70\mu\text{m}$) for a Gr/NMC chemistry. They observed a significant capacity loss when using the thicker cells at C-rates of C/2 due to poor kinetics. The authors suggest that the proposed thick electrodes could be advantageous for certain applications where a continuous low C-rate is required.

Transport properties, ionic and electronic conductivity have all been shown to have a significant impact on lithium ion battery performance. Corroborating the study by Singh et al. [14], results presented by Doyle and Newman [15] highlight that thicker less porous electrodes are a better choice for applications that require a long discharge time, whereas thinner electrodes with higher porosity are more suited for high power short discharge applications. The battery power density is related to both ionic and electronic transport rates. Ion transport occurs in both the separator and electrodes and transport resistance can be reduced by either optimising the separator or by reducing the ionic resistance within the electrode [3,16]. It is noteworthy that there is a trade-off between ionic and electronic conductivity and neither electronic nor ionic conductivity in isolation can achieve optimal specific energy or power. The design trade-offs that exist between ionic and electronic conductivity have been quantified in a study by Chen et al. [3].

Increasing the power density of a cell while maintaining the energy density is a common challenge when developing lithium ion batteries. This is particularly an issue when having high energy cells with thick electrodes, as the power reduces due to longer transport length of the ions and electrons. Understanding the 3D distribution of potential, current, reaction rate, temperature, heat generation, state of charge (SOC) and other properties is a pre-requisite in optimising the design and manufacturability of lithium ion batteries for larger scale applications. Much of the research presented within the literature is underpinned by the formulation of new electrochemical–thermal models. Examples of such models can be seen in the literature for high power applications [17], larger cell capacities (e.g. 45 Ah), cell designs with different tab locations [18,19], the modelling of complete battery packs [20], and to study the heat generation from the cell [21] and its relationship to the overall pack level thermal performance [22].

Most electrochemical–thermal models within the literature assume a spatially uniform porosity within the electrode or separator. However, it is known that porosity has an impact on material properties such as, conductivity, heat capacity and density. It is argued therefore that an optimised spatial variation of porosity within the electrode could enable a more uniform temperature distribution within the cell [7]. The spatial variations in porosity have not been extensively covered within the literature for battery applications [23–25]. Relevant studies include Chiang et al. [23], who have developed a bipolar device with a graded porosity structure. The authors claim that such structures can improve transport properties by removing tortuosity and reducing diffusion distance. Ramadesigan et al. [24] employ a 1D analytical model to optimise the spatial porosity profile across the electrode, for a porous positive electrode made of lithium cobalt oxide. They found that for a fixed amount of active material, optimal grading of the porosity could decrease the ohmic resistance by circa: 15–33%.

Golmon et al. [25] optimised the design properties, porosity and radii distributions with respect to the stress level in the cathode particles. They performed their simulations for a LiMn_2O_4 cathode through the use of half-cell models in addition to a carbon anode fuel cell model. They found that porosity variability had a higher impact on energy capacity than particle radii. Moreover, the improvement in capacity that came from a graded porosity design was in the order of 22% higher than that of a non-graded cell. In addition to the battery domain, the benefits of varying the porosity of the electrode are being actively studied for fuel cell applications as well. For example, recent results highlight that a non-uniformly dispersed porosity of gas diffusion layers (GDL) can lead to a better water management within Polymer Exchange Membrane (PEM) fuel cells [26–28].

This study aims to extend the research, discussed above, by investigating the impact of multi-layered porosity distribution on the electrical and thermal performance of batteries of different cathode chemistries such as LFP or NMC which has not been reported before. To facilitate this study, for the first time a coupled 3D full cell model containing both electrodes is developed. The model enables the authors to investigate the spatial variation along the battery height which is presented here for the first time. To further increase the accuracy of the model the electrochemical model is coupled with a thermal model by considering the porosity dependency of the thermal parameters which has not been considered in the previous works.

The paper is structured as follows: Section 2 discusses in greater depth the formulation of the problem statement and the different use cases that form the basis of the optimisation study. Section 3 defines the creation of a reference model that is validated against both electrical and thermal data presented within the literature. Sections 4–6 present simulation results for the different electrode porosity profiles. Section 7 discusses a new case study containing a high energy cell. Further work and conclusions are discussed in Sections 8 and 9, respectively.

2. Problem statement

Electrode porosity is defined as the volume of pores, which are filled with electrolyte, relative to the volume of the bulk electrode or solid phase:

$$\varepsilon_s + \varepsilon_e = 1 \quad (1)$$

$$\varepsilon_e = \frac{V_e}{V} = \frac{V_e}{V_s + V_e} \quad (2)$$

where (ε_e) and (ε_s) are the porosity (volume fraction of electrolyte) and volume fraction of the solid phase, respectively. The term (V) defines the total volume of the electrode, (V_e) and (V_s) are the volume of the electrolyte and the volume of the active material, respectively, and can be further defined as follows:

$$V_e = \varepsilon_e \cdot V \quad (3)$$

$$V_s = (1 - \varepsilon_e) \cdot V = \varepsilon_s \cdot V \quad (4)$$

Porosity is affected by microstructural parameters that include particle size, particle packing, particle shape and the distribution of particle sizes. A common assumption employed is to simplify the solid electrode material to a collection of spheres with identical particle sizes [22,29,30]. Under this assumption the volume and weight of the active material (solid phase) is equal to:

$$V_s = n_p \times \left(\frac{4}{3} \pi r_p^3 \right) \quad (5)$$

$$m_s = \rho_s \cdot V_s \quad (6)$$

where (n_p) denotes the number of particles and (r_p) the radius of particles within the solid phase. The terms (m_s) and (ρ_s) denote the weight and density of the active material, respectively. In this study, two scenarios for the spatial variation of porosity are investigated with respect to a fixed total weight of active material. From Eqs. (4) and (6), it can be seen that the weight of the electrode can be modified by changing either the relative porosity or total volume of the electrode. The two scenarios that form the basis of this study are defined below:

1. Varying the porosity across the electrode thickness for a fixed average porosity.
2. Varying the porosity in the electrode height for a fixed average porosity.

2.1. Understating the effect of a porous structure on cell thermal properties

To avoid the complication and computational requirements of pore scale modelling of the porous structure, macro homogeneous models are used to obtain effective transport properties. Similar modelling assumptions have been adopted in comparable studies [31–34]. Bruggeman's relationship has commonly been used to correlate and model effective transport

Table 1

Thermal properties of the 10 Ah LFP lithium ion battery [38,39].

Materials	Density, ρ (kg m ⁻³)	Heat capacity, C_p (J (kg K) ⁻¹)	Thermal conductivity, K (W (mK) ⁻¹)	Electronic conductivity, σ (S m ⁻¹)	Ionic conductivity κ (S m ⁻¹)
Negative electrode	2223	641	1.08	100	
Positive electrode	1500	800	1.48	0.5	
Electrolyte	1210	1518	0.099		(12)

kinetics as well as effective conductivities within batteries [35]. The Bruggeman relationship relates tortuosity with porosity as [36]:

$$\tau = \varepsilon_e^{1-brugg_n} \quad (7)$$

where $brugg_n$ is the Bruggeman coefficient. For a system composed of continuous conductive phase such as liquid electrolyte, mixed with spherical particles of uniform size, the parameter has been shown empirically to have the value of 1.5 and represents a common assumption employed in studies that undertake battery simulation, for example [37]. However, for non-spherical particles, the exponent has been found by experiments to have a higher value than 1.5 [35]. Therefore $brugg_n = 1.5$ was deemed to be a reasonable assumption within this study.

The terms (κ) and (κ^{eff}) are the intrinsic and the effective ionic conductivity of the electrolyte, respectively, and can be defined as:

$$\kappa^{eff} = \frac{\kappa \cdot \varepsilon_e}{\tau} = \varepsilon_e^{brugg_n} \cdot \kappa \quad (8)$$

Similarly, the relationship between the intrinsic diffusivity (D_e) and the effective diffusivity (D_e^{eff}) of the electrolyte within a porous structure is expressed as:

$$D_e^{eff} = \frac{D_e \cdot \varepsilon_e}{\tau} = \varepsilon_e^{brugg_n} \cdot D_e \quad (9)$$

From Eqs. (8) and (9) it can be seen that an increase in electrode porosity will improve the conductivity and the diffusion of lithium ions within the electrolyte. The relationship between the intrinsic electronic conductivity (σ) and the effective electronic conductivity (σ^{eff}) of the solid phase is given by [35]

$$\sigma^{eff} = \frac{\sigma \cdot \varepsilon_s}{\tau} = \varepsilon_s^{brugg_n} \cdot \sigma \quad (10)$$

As the level of porosity increases the electronic conductivity of the solid phase decreases as less active material is available for charge transport within the solid phase. To calculate the thermal properties of the electrode, the porous structure can be simplified to a structure with a mixture containing two phases. The thermal properties of the porous structure (electrode or separator) is therefore defined as:

$$\varphi = \varphi_s(1 - \varepsilon_e) + \varphi_e \varepsilon_e = \varphi_s \varepsilon_s + \varphi_e \varepsilon_e \quad (11)$$

where (φ) is the thermal conductivity (K), heat capacity (C_p) and density (ρ). The subscripts 's' denote the solid phase (electrodes and the separator), and 'e' represents the electrolyte. The thermal properties of the lithium ion battery with LiFePO₄ cathode chemistry that has been used within this study are summarised in Table 1.

Ionic conductivity of the electrolyte (κ) is defined as:

$$\begin{aligned} \kappa = & 1.12 \times 10^{-4}(-8.2488 + 0.053248T - 2.9871 \times 10^{-5}T^2 + 0.26235C_e - 9.3063 \times 10^{-3}C_e T \\ & + 8.069 \times 10^{-6}C_e T^2 + 0.22002C_e^2 - 1.765 \times 10^{-4}C_e^2 T) \end{aligned} \quad (12)$$

where (C_e) is the lithium concentration in the electrolyte and (T) identifies the operating temperature of the battery.

2.2. Use cases for electrode optimisation

The following use cases are presented to study the impact of varying the porosity of the cathode on cell performance. The scenarios are: (1) a multi-layered structure of the porosity across the electrode thickness and (2) a multi-layered structure of the porosity across the electrode height, as presented in Fig. 1(a) and (b). As discussed above, variations of (ε_s) will impact a number of material properties, such as the ionic conductivity (κ), electronic conductivity (σ), lithium diffusion coefficient in the electrolyte (D_e), thermal conductivity (K), heat capacity (C_p) and finally the density (ρ). For each use case, the specific energy (W h/kg), the specific power (W/kg) and temperature profile along the surface of the cell are quantified.

2.2.1. Use case 1: a layered structure of porosity across the electrode thickness

Within this case study, the thickness of the electrode was divided into discrete layers with N zones, each with a constant value of ε_s (see Fig. 1a). The average porosity of the electrode can be defined as follows:

$$\varepsilon_{s,ave} = \frac{1}{L_{pos}} \sum_{i=1}^n (\varepsilon_{s,i} \times t_i) \quad (13)$$

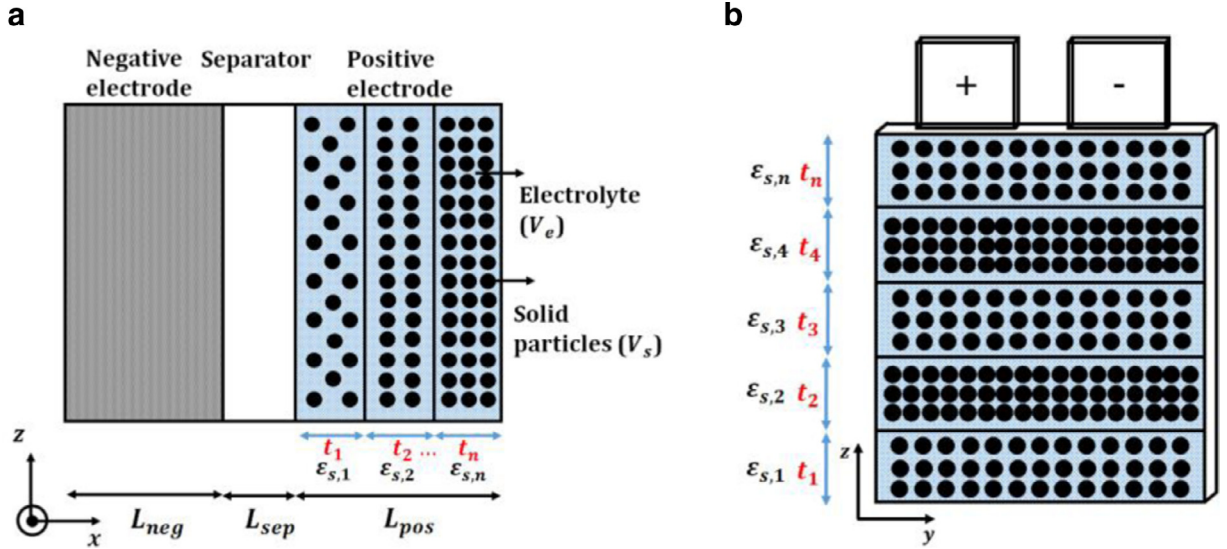


Fig. 1. (a) Multi-layered structure of porosity across the electrode thickness, (b) multi-layered structure of active volume fraction across the cathode height.

where (L_{pos}) defines the thickness of the positive electrode and t_i is the thickness of each of the N layers. According to Chiang et al. [23], the volume fraction of the active material can typically average between 30 and 90%, while the preferred value is between 50 and 80%. Given this parameter range, within the current study, $\epsilon_{s,pos}$ was varied between 0.3 and 0.73. Ramadesigan et al. [24] have optimised the performance of the battery by applying a spatially varying porosity. They proposed that the choice of $N=5$ layers across the electrode thickness provides a good trade-off between the performance improvement within the cell and manufacturing complexity of realising the final design. They reported the optimised porosity values for lithium cobalt oxide comprising of 6 discrete layers. In this study, 6 discrete zones with similar thickness, different porosities have been applied for all test cases. The optimised porosity profile suggested by Ramadesigan et al. [24] was a non-linear multi-layered profile. However, there is insufficient information within the literature to properly understand if this form of distribution is optimum and transferable to other cell chemistries with different capacity ratings. In this case study, porosity variation across the electrode thickness from one layer to another was varied both linearly and non-linearly.

2.2.2. Use case 2: layered structure of porosity along the electrode height

For this design case the height of the electrode is divided to N layers with different porosities, as shown in Fig. 1b.

The average volume fraction of active material in the electrode can be expressed as:

$$\epsilon_{s,ave} = \frac{1}{H} \sum_{i=1}^n (\epsilon_{s,i} \times t_i) \quad (14)$$

where (n) is the number of layers and (t_i) indicates the thickness of each layer. The number of layers employed within the simulation, was set to 4. Similarly, the porosity variation across the electrode thickness from one layer to another was varied both linearly and non-linearly.

3. Validation of the coupled thermal–electrochemical model

A full 3D electrochemical–thermal model is developed for a single electrode-pair of a lithium ion battery with LFP cathode. Each pair is assumed to be a sandwiched model of different layers: a negative current collector, a negative electrode, a separator, a positive electrode and a positive current collector. The current model is extension of the previously developed and validated 1D model discussed in [40], which is based on a similar, experimentally validated model presented within Li et al. [38]. The input to the model is load current, geometrical design parameters, material properties and ambient operating temperature. Through the proposed case studies, discussed in Section 2, only one of the design variables was modified: the volume fraction of the active material, denoted as $(\epsilon_{s,pos})$. As explored in the previous section, changing (ϵ_s) will in turn change other properties such as ionic conductivity (κ) , electronic conductivity (σ) , lithium diffusion coefficient in the electrolyte (D_e) , thermal conductivity (K) , heat capacity (C_p) and finally the density (ρ) . The outputs from the model are the responses of the cell to the load, i.e. terminal voltage (V) , generated heat (Q) , temperature profile $(^\circ\text{C})$ and SOC. Additional internal variables include: lithium concentration in the electrodes and the separator, potential distribution of different phases, reaction current, electronic and ionic current. The primary motivation for using Li et al.'s model [38] for verification is because the authors have presented a complete set of electrochemical parameters for the cell along with a definition

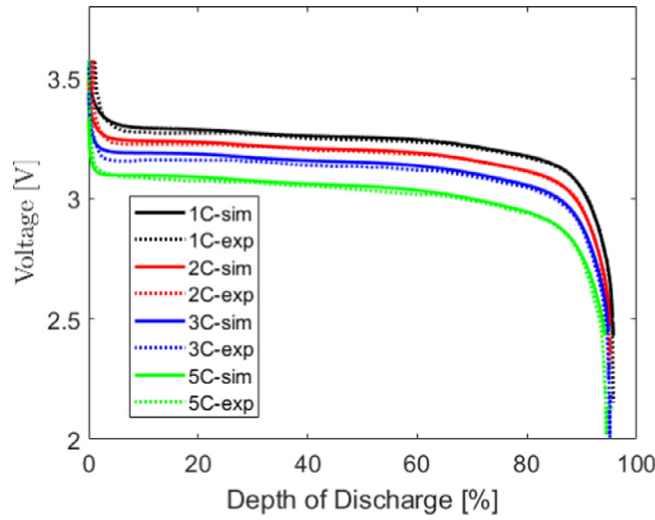


Fig. 2. Discharge curve of the 10 Ah pouch cell at different C-rates, at room temperature, $T_{amb} = 25\text{ }^{\circ}\text{C}$ with natural cooling condition.

of parameter variations with temperature. Since the electrochemical model contains temperature dependent variables, coupling it with a thermal model yields more accurate results. Furthermore, the model presented in [38] has been validated using experimental data. The parameterisation data and experimental results presented within [38] allow for the creation of a Reference Model to ensure the accuracy and robustness of the model, before proceeding with the two use case studies defined within Section 2.2. The developed model is based on P2D electrochemical–thermal equations which are solved in COMSOL Multiphysics for a 3D cell geometry. A segregated time dependent solver has been used for all the simulations. A cut off voltage of 2.5V has been used to terminate the cell discharge. The output from the model shows a high degree correlation with the results published within [38] in terms of the terminal voltage response when the cell is discharged, the surface temperature gradient and other internal parameters (e.g. local SOC, lithium concentration, potential and internal current). Further validation details are discussed below.

3.1. Discharge curve

The terminal voltage discharge curve for the 10 Ah LFP pouch cell under 1C to 5C discharge current rate at ambient temperature ($T = 25\text{ }^{\circ}\text{C}$) is presented in Fig. 2 and shows a good agreement between the simulation results and the experimental data. The simulation results are generated by the 3D COMSOL model used in this study and the experimental data are those reported by Li et al. [38].

3.2. Reference Case—model design parameters

The initial design parameters of the Reference Case are those reported by Li et al. [38], presented in Table 2. The following parameters have been employed to fully define the reference model.

4. Extending the validated model—the Reference Case study

The validated model is used as a Reference Case to evaluate the specific energy, specific power, total heat generation and the resulting temperature profile. The model is further applied for use cases with multi-layered porosity profile, to account for any changes in the energy or power that may arise from such a porosity distribution.

Specific energy (E_{cell}) and specific power (P_{cell}) are defined as [41]:

$$E_{cell} = 1/m_{cell} \int_0^{t_{dis}} V_t(t) \cdot I \cdot dt \quad (24)$$

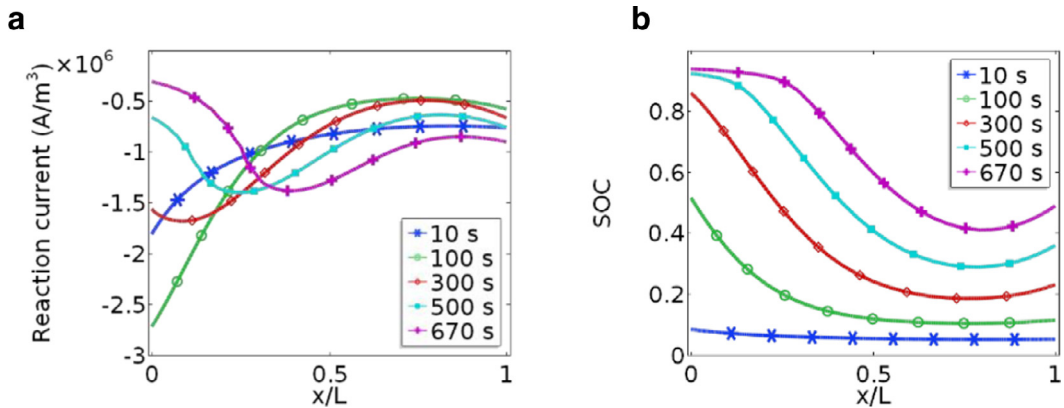
$$P_{cell} = 1/(t_{dis} \cdot m_{cell}) \int_0^{t_{dis}} V_t(t) \cdot I \cdot dt \quad (25)$$

where m_{cell} is the total weight of the cell and t_{dis} is the final time when the cell reaches the cut off voltage of 2.5.

Table 2

Parameter values for the 10 Ah LFP pouch cell [38].

Parameter	Negative electrode	Separator	Positive electrode
Thickness, L (μm)	34	25	70
Particle size, r_p (μm)	3.5		0.0365
Volume fraction of the active material, ε_s	0.55		0.43
Volume fraction of the electrolyte, ε_e	0.33	0.54	0.332
Maximum lithium concentration in the solid phase, $C_{s, \max}$ (mol m^{-3})	31,370		22,806
Electrolyte lithium concentration, $C_{e, \max}$ (mol m^{-3})		1200	
Bruggeman porosity exponent, $brugg_n$	1.5	1.5	1.5
Dynamic parameters			
Lithium diffusion coefficient in the negative electrode, $D_{s, \text{neg}}$ ($\text{m}^2 \text{s}^{-1}$)	$D_{s, \text{neg}} = 3.9 \times 10^{-14} \exp\left(\frac{-35000}{R}\left(\frac{1}{T} - \frac{1}{298.15}\right)\right)$		
Lithium diffusion coefficient in the positive electrode, $D_{s, \text{pos}}$ ($\text{m}^2 \text{s}^{-1}$)	$D_{s, \text{pos}} = \frac{1.18 \times 10^{-18}}{(1+y)^{1.6}} \exp\left(\frac{-35000}{R}\left(\frac{1}{T} - \frac{1}{298.15}\right)\right)$		
Lithium diffusion coefficient in the electrolyte, $D_{e, \text{neg}}$ ($\text{m}^2 \text{s}^{-1}$)	$D_e = 1e - 4 \times 10^{-4.43}\left(\frac{54.0}{1-229.0-0.05c_e}\right) 2.2 \times 10^{-4c_e}$		
Reaction rate in the negative electrode, k_{neg} (m s^{-1})	$k_{\text{neg}} = 3 \times 10^{-11} \exp\left(\frac{-20000}{R}\left(\frac{1}{T} - \frac{1}{298.15}\right)\right)$		
Reaction rate in the positive electrode, k_{pos} (m s^{-1})	$k_{\text{pos}} = 1.4 \times 10^{-12} \exp(-y) \exp\left(\frac{-30000}{R}\left(\frac{1}{T} - \frac{1}{298.15}\right)\right)$		
Open circuit potential of the negative electrode	$U_{\text{neg, ref}} = 0.6379 + 0.5416 \exp(-305.5309x) + 0.044 \tanh\left(-\frac{x-0.1958}{0.1088}\right) - 0.1978 \tanh\left(\frac{x-0.0117}{0.0529}\right) - 0.0175 \tanh\left(\frac{x-0.5692}{0.0875}\right)$		
Open circuit potential of the positive electrode	$U_{\text{pos, ref}} = 3.4323 - 0.4828 \exp(-80.2493(1-y)^{1.3198}) - 3.2474 \times 10^{-6} \exp(20.2645(1-y)^{3.8003}) + 3.2482 \times 10^{-6} \exp(20.2646(1-y)^{3.7995})$		
Entropy change of the negative electrode	$\frac{dU_{\text{neg}}}{dT} = 344.1347148 \times \frac{\exp(-32.9633287x+8.316711484)}{1+0.749.07566003 \exp(-34.79099646x+8.887143624)} - 0.8520278805x + 0.362299229x^2 + 0.2698001697$		
Entropy change of the positive electrode	$\frac{dU_{\text{pos}}}{dT} = -0.35376y^8 + 1.3902y^7 - 2.2585y^6 + 1.9635y^5 - 0.98716y^4 + 0.28857y^3 - 0.046272y^2 + 0.0032158y - 1.9186 \times 10^{-5}$		

**Fig. 3.** The evolution of: (a) the reaction current, (b) the local SOC at the positive electrode during 5C discharge, Reference Case. $x=0$ is the separator/electrode interface, while $x/L=1$ represents the electrode/current collector interface.

4.1. Reaction current and SOC

The reaction current and the local SOC of the 10 Ah LFP lithium ion battery are shown in Fig. 3(a) and (b), respectively.

The current distribution is through the positive electrode thickness during a complete 5C discharge. L is electrode thickness, where $x=0$ represents the separator/electrode interface while $x/L=1$ is the electrode/current collector interface. At the early stages of the discharge process, the peak value of the reaction current occurs at the separator/positive electrode interface and moves towards the electrode/current collector interface as the discharge proceeds. This happens when the effective conductivity of the solid phase (σ^{eff}) is higher than that of the liquid phase (κ^{eff}), i.e. ($\sigma^{\text{eff}} > \kappa^{\text{eff}}$). In general, the peak location depends upon the magnitude of σ^{eff} compared to κ^{eff} [39,42]. In addition, the ionic current density is always maximum at the separator/electrode interface whereas the maximum value for electronic current is seen at the electrode/current collector interface.

The local SOC is defined as the ratio of lithium ion concentration at the surface of the active material to the maximum lithium concentration of the bulk electrode. Hence, by definition the SOC profile follows the same trend as the lithium concentration presented in Fig. 3b. Within the positive electrode, the particles near to the separator firstly approach the fully charged state. This can be attributed to the reaction current which itself is a function of conductivity of the different

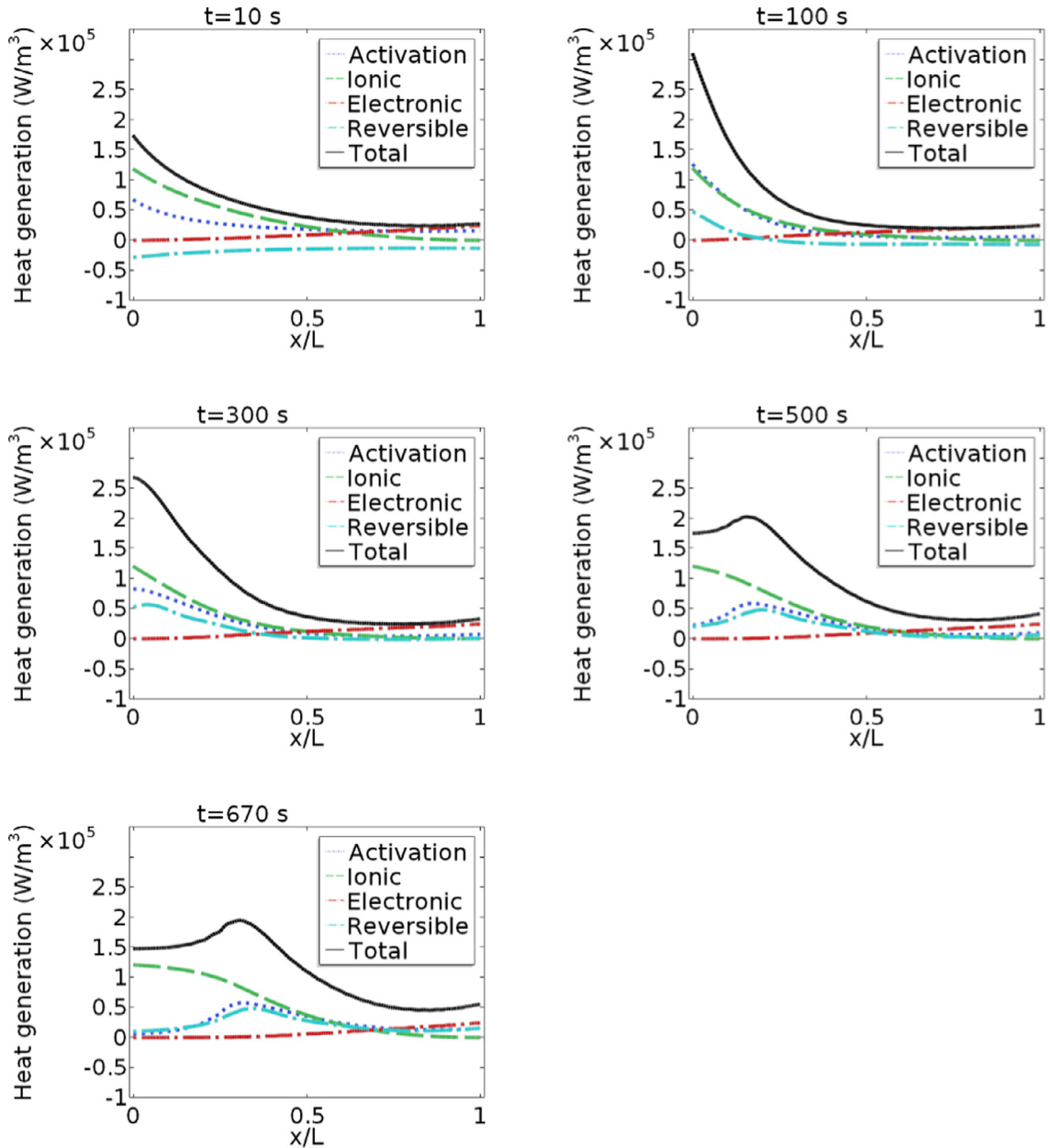


Fig. 4. Heat evolution at the positive electrode during 5C discharge at $t = 10$ s, $t = 100$ s, $t = 300$ s, $t = 500$ s and $t = 670$ s, Reference Case. $x = 0$ is the separator/electrode interface, while $x/L = 1$ represents the electrode/current collector interface.

phases. This is shown in Fig. 3(a) and (b) and is consistent with theoretical predictions [39]. The observed dip in the SOC profile versus x/L is due to the non-homogenous distribution of the reaction current.

4.2. Heat generation

The amount of activation heat is proportional to the reaction current density and the surface over-potential. Generally, the average value for activation heat is known not to change much within the positive electrode during the electrochemical reaction. In this example, it ranges from 0.239 W/m^3 at $t = 10$ s to 0.253 W/m^3 at the end of discharge event ($t = 670$ s) when the cut-off voltage of 2.5 V is reached. The peak for the reaction heat appears at the electrode/separator interface during the early period of the discharge, until $t = 300$ s, and then moves towards the electrode/current collector interface as it proceeds to the end of the discharge, see Fig. 4. As shown in Fig. 3a, a change in the location of the maximum reaction heat is due to a shift in the location of the reaction current as well as a change in the location of the electrochemical over-potential [43].

The ohmic heat (Q_{ohm}), which is a combination of ionic ($Q_{ohm,i}$) and electronic heat ($Q_{ohm,e}$), is caused by the resistance against the flow of electrons in the solid phase as well as lithium ions in the electrolyte phase. The ionic heat is calculated using the formula:

$$Q_{ohm,i} = \sigma^{eff} \nabla \phi_e \nabla \phi_e \text{ or } i_e^2 / \sigma^{eff} \quad (26)$$

where κ^{eff} is the effective ionic conductivity, ϕ_e is the electrolyte potential and i_e represents the ionic current.

The average value for the ionic heat is around $0.284 \times 10^5 \text{ W/m}^3$ at the beginning of the discharge, and reduces slightly to $0.225 \times 10^5 \text{ W/m}^3$ at $t=90 \text{ s}$ and increases again monotonically until the end of the discharge event to $0.509 \times 10^5 \text{ W/m}^3$ at $t=670 \text{ s}$. The spatial profile of the ionic heat is related to the potential gradient of the electrolyte and as a consequence, to the local current density within the electrolyte. It can be seen from Fig. 4 that the location for the maximum ionic heat is at the separator/positive electrode interface during the entire discharge process. That is in agreement with the ionic current profile through the electrode thickness.

The electronic ohmic heat is calculated as:

$$Q_{ohm,e} = \sigma^{eff} \nabla \phi_s \nabla \phi_s \text{ or } i_s^2 / \sigma^{eff} \quad (27)$$

where i_s is the electronic current density. Unlike the ionic heat, the electronic heat increases slightly during the early period of the discharge, until $t=110 \text{ s}$, then decreases monotonically until the end of discharge, with the minimum value of $0.080 \times 10^5 \text{ W/m}^3$ at $t=675 \text{ s}$. Generally, as reported within [43], the electronic heat is much less than the ionic heat due to the much larger ionic charge resistance in comparison to the electronic resistance. However, because of the low electronic conductivity of the LFP material, in this example, the electronic heat is relatively high for this specific cell. Hence around 13–35% of the total ohmic heat generation within the cathode is attributed to electronic heat with the remainder coming from ionic heat. The peak for the electronic heat appears at the positive electrode/current collector interface where the electronic current is at a maximum.

The reversible heat of the electrodes is due to entropy change and is equal to:

$$Q_{rev} = -I \cdot T \cdot \frac{dU}{\partial T} \quad (28)$$

where $\frac{dU}{dT}$ is potential deviation of electrodes as a result of entropy changes, as displayed in Table 2. The contribution of the irreversible electrochemical reaction heat, ohmic heat (electronic and ionic) and reversible heat to the total heat generation of the positive electrode is about 23–55%, 50–78% and 19–29%, respectively. As shown in Fig. 4, initially the location of the maximum heat is at the separator/cathode interface from the beginning of the discharge process until $t=300 \text{ s}$. As the discharge event progresses, the peak shifts towards the positive current collector interface, as previously described. For this particular cell, operating at a 5C discharge, the area near to the separator generates most of the heat while the part of the electrode closer to the current collector does not.

Within the next section, the different use cases, defined in Section 2.1, are further studied to understand the causality between variations in ε_s within the electrode and how this affects the charge resistance and spatial profile of the heat generation as well as the internal electrochemical parameters for the cell.

5. Simulation results—layered structure of porosity across the electrode thickness

As discussed within [39], Ohmic resistance is a major source of voltage drop, especially within thicker electrodes. Improved ion transport kinetics within a composite structure such as an electrode can be achieved by adjusting the ionic conductivity relative to the current distribution. As the ionic current, can be higher near the electrode and separator interface, a higher ionic conductivity in this region can improve the transport rate. This means that having a higher porosity near to the separator can help improve power density, while a higher fraction of active material in the depth of the electrode (towards the current collector) helps to retain a higher energy capability [23].

The following case study indicates the variation of the electrode volume fraction versus the dimensionless distance across the electrode (Table 3). A distance of $x=0$ indicates the separator/positive electrode interface, while $x/L=1$ represents the positive electrode/current collector interface.

The simulation results of the different cases are presented in Table 4.

In case studies 1–5, the minimum ε_s is at the electrode/separator interface, while the maximum ε_s is close to the current collector. In case studies 6–10, the distribution of ε_s is in the reverse direction, as shown in Table 3. The results of the first group (cases 1–5) do not highlight significant improvement in battery performance, in terms of either specific energy or power density. For the best case scenario (case 3), the energy and power increased by 0.33% and 0.44%, respectively. Moreover, the maximum variation of the peak temperature compared to the Reference Case is approximately 0.9°C .

Even though no significant improvement has been observed by linear and non-linear distribution of the porosity, porosity distribution in the reverse direction (cases 6–10), can deteriorate cell performance significantly. Hence by having a high active volume fraction near the separator and low volume fraction near the current collector, it is impossible to improve performance of a battery, regardless of its chemistry or size. The results of case studies 6–10 confirm the significant loss in both energy and power along with a higher peak temperature and temperature gradient. For the worst-case scenario, e.g. case 8, the specific energy and the specific power of the battery have decreased by circa: 36% and 4.1%, respectively.

Table 3

Active volume fraction distribution of different case studies across the thickness of the positive electrode. L is the thickness of the positive electrode and $x = 0$ is the separator/electrode interface, while $x/L = 1$ represents the electrode/current collector interface.

Case study	$\varepsilon_{s,1}$ $x/L = 0$	$\varepsilon_{s,2}$	$\varepsilon_{s,3}$	$\varepsilon_{s,4}$	$\varepsilon_{s,5}$	$\varepsilon_{s,6}$ $x/L = 1$
Case 1	0.3	0.38	0.46	0.54	0.62	0.7
Case 2	0.4	0.44	0.48	0.52	0.56	0.6
Case 3	0.35	0.37	0.43	0.5	0.6	0.7
Case 4	0.40	0.42	0.45	0.50	0.57	0.66
Case 5	0.40	0.41	0.43	0.48	0.56	0.72
Case 6	0.70	0.62	0.54	0.46	0.38	0.3
Case 7	0.60	0.56	0.52	0.48	0.44	0.40
Case 8	0.73	0.61	0.50	0.43	0.37	0.35
Case 9	0.66	0.57	0.50	0.45	0.42	0.4
Case 10	0.72	0.56	0.48	0.43	0.41	0.4

Table 4

The simulation results of scenario 1b, positive electrode.

Case study	E_{cell} (W h/kg)	P_{cell} (W/kg)	T_{max} (°C)	ΔT (°C)
Reference Case	130.25	694.25	46.30	2.77
1	130.76	696.39	47.18	2.92
2	130.52	696.82	47.06	2.92
3	130.69	697.34	47.09	2.91
4	130.69	696.93	46.93	2.93
5	130.83	696.68	46.90	2.93
6	121.42	658.71	60.02	2.88
7	129.17	689.63	50.35	2.91
8	83.17	665.38	53.33	2.83
9	127.14	681.83	52.98	2.85
10	108.74	632.80	55.42	2.92

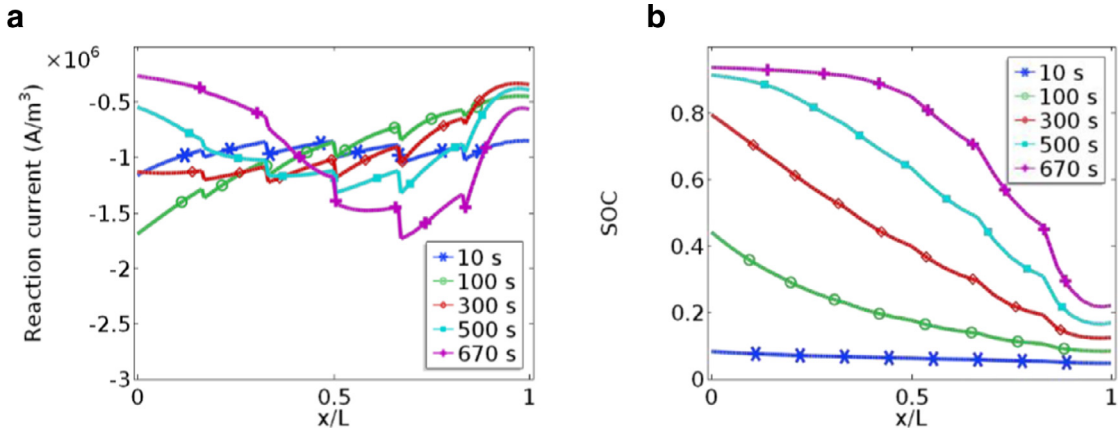


Fig. 5. Spatial distribution of: (a) the reaction current, (b) the local SOC at the positive electrode during the 5C discharge process at $t = 10$ s, $t = 100$ s, $t = 300$ s, $t = 500$ s and $t = 670$ s, case 3. $x = 0$ is the separator/electrode interface, while $x/L = 1$ represents the electrode/current collector interface.

In terms of the peak temperature, case 6 is the worst condition, with a 13.72 °C increase in peak temperature. Case 3 has the highest power density among the test cases. Even though the power variation of the different test cases in group 1 is almost negligible. The following sub-sections compare in greater depth the reaction current, SOC and heat generation of case 3 from group 1 with those of the Reference Case during the discharge event.

5.1. Reaction current and SOC

The spatial variation of the reaction current and SOC within the cathode for case 3 is shown in Fig. 5(a) and (b), respectively. At the beginning of the reaction, the reaction current is comparable with that of the Reference Case (see Fig. 3a). However, as it proceeds to the end of discharge the local variation within the current density increases and generates a larger charge gradient across the positive electrode.

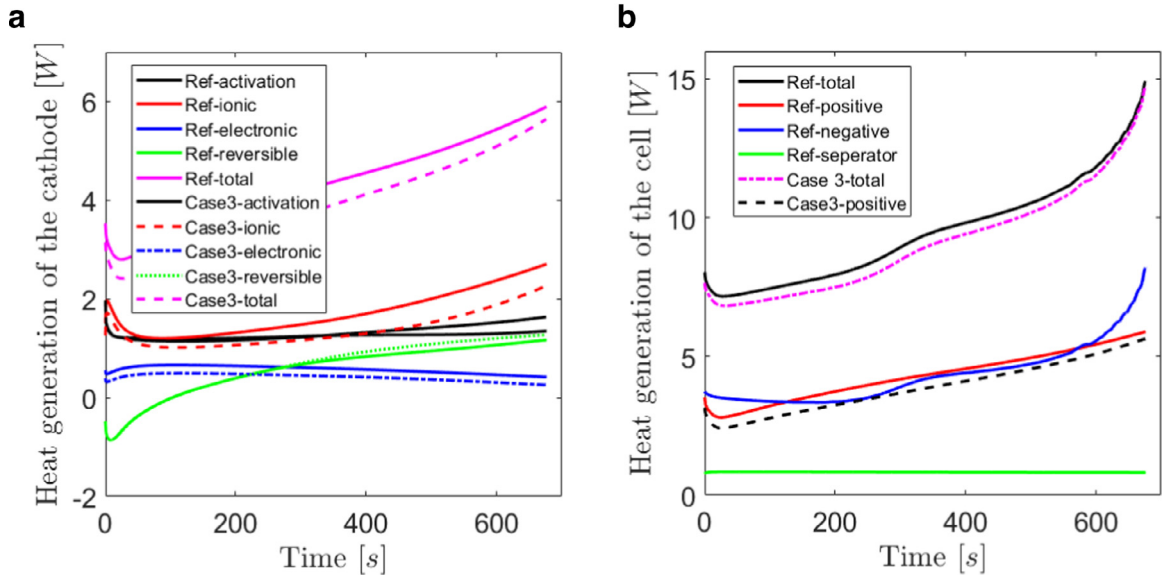


Fig. 6. (a) Comparison between heat generation (activation, electronic, ohmic, reversible and total) of case 2 (scenario 1a) and Reference Case, at the positive electrode; (b) total heat generation of the cells during 5C discharge process.

The same phenomenon is true when reviewing the SOC results. As shown in Fig. 5b, the local variation of SOC for case 3 is much higher compared to the Reference Case (Fig. 3b). This is particularly true at the end of the discharge event and causes a non-uniform utilisation of the active material which is not desirable. The reason for this is due to the increased local ionic resistance to the charge transfer within the electrode regions closer to the current collector that exhibit a relatively high volume fraction of active material.

5.2. Heat generation

Fig. 6a compares the heat generation of the different sources for case 3 with the heat generation modes of the Reference Case over the same time interval. The values represent the average heat evolution of the positive electrode during the discharge. The results show that for case 3, the activation heat, the ohmic heat (both ionic and electronic) decreases with the multi-layered porosity structure that in turn leads to a significant reduction of total heat generation. The ionic heat which is the major contributor to heat generation decreases by 11–24% compared to the Reference Case during the 5C discharge process. The reduction in electronic heat is approximately 28–38% over the discharge. From Fig. 6, the activation heat appears to be unchanged during the electrochemical reaction until $t = 345$ s. Immediately after this time, it begins to increase while in the Reference Case it remains almost constant. The underlying reason for this is because within case 3 the activation over-potential increases after this point, even though the reaction rate is lower. Combining all the heat generation modes together, the total heat generation of the positive electrode for case 3 reduces by 4.2–14%, with a time averaged value of 10.4% compared to the Reference Case presented in Fig. 6a. The heat evolution of the positive electrode is almost 45% of the total heat generation of the battery as shown in Fig. 6b. considering this, a total heat reduction of 4.2% is obtained for the whole cell.

6. Simulation results—layered structure of porosity along the electrode height

This scenario elaborates a multi-layered porosity distribution along the z axis of the electrode. Six case studies were investigated. These can be divided into two groups; group 1 with low ε_s at the top and high ε_s at the bottom of the cell (test cases 1–3) and the second group with a reverse distribution, i.e. with high ε_s at the top and low ε_s at the bottom. The profile of the porosity from minimum to a maximum value is either linear or non-linear as shown within Table 5. The average volume fraction of the layers is 0.5, equal to the overall volume fraction of the Reference Case model defined in Section 3.2.

In general, the test cases from group 1 show an improved battery performance from those represented within group 2, see Table 6. However, the authors acknowledge that the differences are not significant. The only exception to this is test case 6 for which the discharge process terminated after a very short time ($t = 40$ s) because the terminal voltage of the cell dropped below the threshold value of 2.5 V. It is for this reason that value of E_{cell} is very low. From the results obtained from group 1, it seems that the ionic current at the top of the cell where the active volume fraction is maximum is very close to zero, meaning that the low porosity region is a barrier for ion transport and the electrochemical reaction cannot proceed in

Table 5

Multi-layered distribution of the active material volume fraction at the positive electrode across the height of the cell, case study 2, scenario 2b.

Case study	$\varepsilon_{s,1}$ $y=0$	$\varepsilon_{s,2}$	$\varepsilon_{s,3}$	$\varepsilon_{s,4}$ $y=H$
Case 1	0.7	0.56	0.44	0.3
Case 2	0.6	0.53	0.47	0.4
Case 3	0.71	0.49	0.42	0.38
Case 4	0.3	0.44	0.56	0.7
Case 5	0.4	0.47	0.53	0.6
Case 6	0.38	0.42	0.49	0.71

Table 6

Simulation results of different test cases, scenario 2b.

Case study	E_{cell}	P_{cell}	T_{max}	ΔT
Reference Case	130.25	694.25	46.30	2.78
1	100.27	694.15	47.40	2.73
	128.63	689.08	51.89	3.26
2	104.21	694.72	49.42	2.9
3	100.24	693.98	49.54	3.43
4	128.11	689.04	50.74	6.28
	7.90	710.86	29.64	3.07
5	100.27	694.15	47.40	2.73
6	128.63	689.08	51.89	3.26

that region. Among the test cases of group 1, cases 1 and 3 show a significant reduction in energy capability (e.g. 23% and 20%, respectively), while maintaining the same power capability as the reference model case. However, case 2 shows a 0.8% power reduction compared to the Reference Case while maintaining the same energy. Moreover, case 2 exhibits the highest temperature within all of the designs options within group 1; equal to 51.9 °C—a 12% increase compare to the Reference Case. The high temperature can partly be attributed to its lower power, as a result of its reduced cell voltage.

Case 2 from group 1 was chosen for further analysis, due to it having the highest specific energy and temperature, and is explored further in the following sub-sections.

6.1. Reaction current and SOC

Fig. 7(a) and (b) presents the spatial distribution of the internal parameters for case 2, similarly Fig. 7(c) and (d) shows the spatial variation of the electrochemical parameters for the Reference Case during the 5C discharge process at a time $t=500$ s. For case 2, the reaction current is minimum at the bottom of the cell where the active volume fraction is highest. This result is consistent with theoretical predictions; as at higher ε_s there is an increased ionic resistance that limits the rate of the electrochemical reaction. From the results obtained, the current seems almost uniform along the rest of the cell where the active volume fraction is lower than 0.6. The cathode SOC, Fig. 7(b), shows a large gradient for case 2, in the order of 53.8% within the electrode that in turn yields a very inconsistent reaction rate as shown in Fig. 7(a). In contrast to case 2, the local variation of SOC is only 1.3% for the Reference Case, accompanied by a much lower gradient for the reaction rate across the electrode surface.

6.2. Temperature

The non-homogeneous distribution of the electrochemical parameters within the positive electrode explains the increased temperature gradient (by approximately 17%) that can be seen in case 2 when compared to the Reference Case. The temperature profile of both cases is shown in Fig. 8. It is noteworthy that with a porosity profile of this shape, not only does the peak temperature and temperature gradient vary, but also the location of the hot spot moves from the positive tab towards to the bottom of the cell. This highlights the correlation of the temperature gradient with electrode design.

6.3. Sensitivity analysis

To investigate the sensitivity of the model to the thermal parameters (ρ , C_p , K), a sensitivity analysis was undertaken. Model outputs such as the temperature of the cell as well as the location of the hot spot were investigated over a wide range of thermal parameters (summarised in Table 7). The results show a small variation of temperature versus the thermal parameters. Moreover, the location of the hot spot was similar to those presented within Section 6.2.

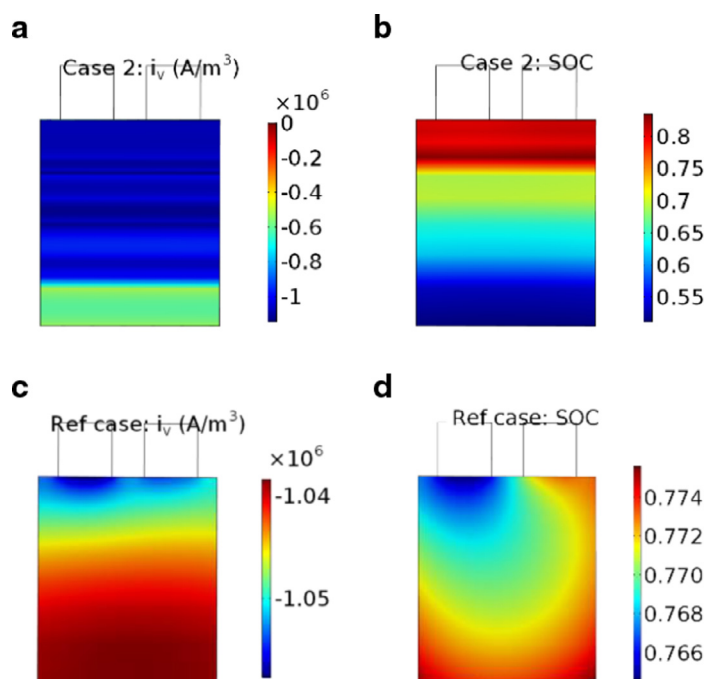


Fig. 7. The spatial variation of the internal parameters during the 5C discharge, at $t=500$ s for case 2 (a, b), (a) the reaction current, (b) the local SOC, and the Reference Case (c, d), (c) reaction current, (d) the local SOC. The left side tab represents the positive tab and the negative tab locates on the right.

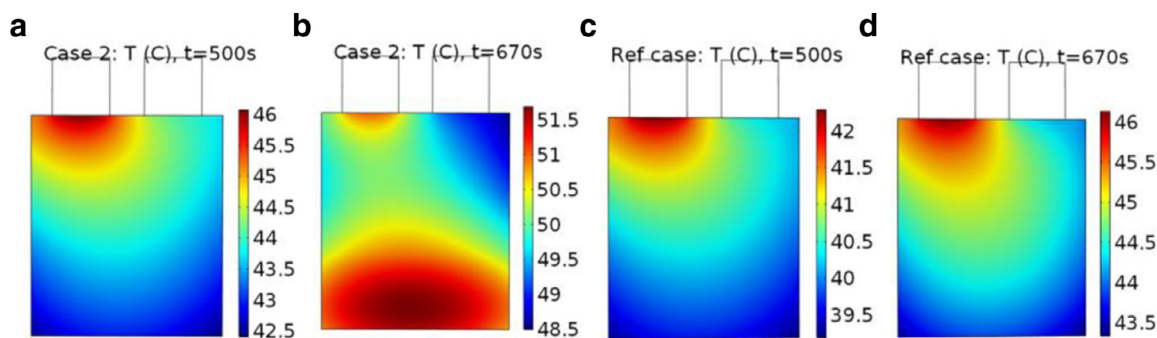


Fig. 8. The temperature profile of the cathode during the 5C discharge, case 2 (a, b), (a) at $t=500$ s, (b) $t=670$ s, Reference Case (c, d), (c) at $t=500$ s, (d) $t=670$ s. The left side tab represents the positive tab and the negative tab locates on the right.

Table 7

The results of the sensitivity study of the thermal model versus thermal properties of the positive electrode, Reference Case.

ρ (kg m^{-3})	T_{\max}	ΔT	C_p ($\text{J (kg K}^{-1}\text{))}$	T_{\max}	ΔT	K (W (mK)^{-1})	T_{\max}	ΔT
1000	46.95	2.7	600	46.6	2.72	1	46.27	2.72
1500	46.28	2.73	800	46.27	2.72	1.48	46.28	2.72
2000	45.61	2.74	100	45.99	2.73	10	46.20	2.60

7. High energy cell

Nano-sized LFP electrodes are well known for their high power capabilities and the results defined within Sections 5 and 6 highlight limited improvement for such cells through multi-layered porosity structure. To extend this research a different cell with 53 Ah capacity was investigated for comparison. The detailed study and optimisation of the cell is defined as a future work, see Section 8. The NMC/graphite cell is made of 111 μm positive electrode along with 202 μm negative electrode. The pertinent design parameters are summarised in Table 8.

Table 8

Key design parameters of the 53 Ah cell with NMC/graphite chemistry.

Parameter	Negative electrode	Separator	Positive electrode
Thickness, L (μm)	202	17	111
Particle size, r_p (μm)	26.2		10.7
Volume fraction of the active material, ε_s	0.58		0.43
Volume fraction of the electrolyte, ε_e	0.32		0.32

Table 9

Simulation results of a multi-layered porosity structure across the thickness of the NMC/graphite cell.

Case study	$\varepsilon_{s,neg}, \varepsilon_{s,pos}$	E_{cell} (W h/kg)	P_{cell} (W/kg)
Reference Case	$\varepsilon_{s,neg} = 0.58, \varepsilon_{s,pos} = 0.43$	254.49	1214.9
Case 1	$\varepsilon_{s,neg} = \begin{cases} \varepsilon_{s,1} = 0.71 \\ \varepsilon_{s,2} = 0.66 \\ \varepsilon_{s,3} = 0.60 \\ \varepsilon_{s,4} = 0.55 \\ \varepsilon_{s,5} = 0.50 \\ \varepsilon_{s,6} = 0.45 \end{cases}, \varepsilon_{s,pos} = 0.43$	275.8	1246.3
Case 2	$\varepsilon_{s,neg} = 0.58, \varepsilon_{s,pos} = \begin{cases} \varepsilon_{s,1} = 0.30 \\ \varepsilon_{s,2} = 0.35 \\ \varepsilon_{s,3} = 0.40 \\ \varepsilon_{s,4} = 0.45 \\ \varepsilon_{s,5} = 0.51 \\ \varepsilon_{s,6} = 0.56 \end{cases}$	242.88	1215.4
Case 3	$\varepsilon_{s,neg} = \begin{cases} \varepsilon_{s,1} = 0.71 \\ \varepsilon_{s,2} = 0.66 \\ \varepsilon_{s,3} = 0.60 \\ \varepsilon_{s,4} = 0.55 \\ \varepsilon_{s,5} = 0.50 \\ \varepsilon_{s,6} = 0.45 \end{cases}, \varepsilon_{s,pos} = \begin{cases} \varepsilon_{s,1} = 0.30 \\ \varepsilon_{s,2} = 0.35 \\ \varepsilon_{s,3} = 0.40 \\ \varepsilon_{s,4} = 0.45 \\ \varepsilon_{s,5} = 0.51 \\ \varepsilon_{s,6} = 0.56 \end{cases}$	271.72	1246.1

Similar to LFP cells, a multi-layered porosity structure across the electrode thickness is applied for the NMC cell and three case studies are presented considering a multi-layered anode, a multi-layered cathode and a combination of both. The case studies and achieved energy and power are presented in Table 9.

The results show that for this specific cell a significant improvement is obtained by a varied porosity structure across the anode. The improvement can be seen within both the energy and the power characteristics of the cell. The gained energy and power compared to the Reference Case is around 8.37% and 2.6%, respectively. The cathode varied porosity does not make an improvement for this cell. One conclusion may be that the porosity structure of the cell is not yet optimised and therefore there is the potential for a performance improvement.

8. Further work

Further analysis is required to fully understand the causality between the porosity distribution within the electrode and whether the power capabilities of the cell can be improved without compromising energy density. This study highlights the effect that a multi-layered porosity structure within the positive electrode may have for different internal parameters as well as quantifying the general performance implications for the battery. While the numerical results presented are only applicable to the specific battery type employed, the authors assert the modelling approach and rationale are transferable to other cell types and chemistries. Further research is required to better understand the transferability of these results to larger cells that have higher energy capacity and increased physical dimensions, potentially operating at higher C-rates. In addition, extending the parameterisation of the model to take account of different electrode chemistries will further highlight if the results presented here are representative of a wider cross-section of cell types. As seen from the results, variations in electrode porosity can impact the value and location of the peak temperature during the discharge event. A further refinement would be to extend the model to include degradation mechanisms within the cell. Example improvements to the model would include representing the solid-electrolyte interface (SEI) growth and its effect on the capacity fade within the battery. Finally, it is suggested that the optimal design should be manufactured, potentially using the new techniques being developed by Grant et al. [44], accompanied by an experimental evaluation of the optimised cell versus an equivalent commercially available cell that has been manufactured using traditional electrode formulation methods.

9. Conclusion

In this study, a 3D electrochemical–thermal model has been developed using COMSOL Multiphysics, in order to investigate the impact of non-homogeneous porosity distribution on cell performance. In order to facilitate a comparison a reference model has been formulated and validated using published data and experimental results presented by Li et al. [38], for a 10 Ah LFP pouch cell.

Two different scenarios have been defined to vary the porosity across the thickness or height of the positive electrode. The scenarios are: (1) a multi-layered structure of the porosity across the electrode thickness and (2) a multi-layered structure of the porosity across the electrode height. The spatial distribution of the internal parameters such as current density, SOC, as well as overall cell performance has been investigated for each case study for different discharge currents.

From the results obtained, varying the porosity distribution increases the inhomogeneity of the electrochemical parameters. Even though no significant improvement has been observed for this specific cell type, the simulation results highlight that a multi-layered porosity distribution along the electrode thickness, with high porosity at the separator/electrode interface, seems to yield the most promising results. For example, case study 2 from scenario 1 showed a reduction in the total heat generation within cathode by approximately 4.2–14% over the discharge event.

Extending this research further, additional studies are currently ongoing in which more significant results may be obtained, for example, by re-parameterising the model to emulate a cell with a thicker electrode, where the impact of ohmic resistance is expected to be higher. In addition, it would be more promising to simulate the performance of a larger cell (both in terms of energy capacity and physical dimensions) operating under a higher C-rate conditions, where the inhomogeneity of the cell is known to be more pronounced. While the numerical results presented are only applicable to the specific battery type employed, the authors assert the modelling approach and rationale are transferable to other cell types and chemistries. An example of a high energy cell with different chemistry types has been presented in Section 7, showing a significant potential for improvement.

Acknowledgements

The research was undertaken as a part of ELEVATE project (EP/M009394/1) funded by the Engineering and Physical Science Research Council (EPSRC).

References

- [1] P.V. Braun, J. Cho, J.H. Pikul, W.P. King, H. Zhang, High power rechargeable batteries, *Curr. Opin. Solid State Mater. Sci.* 16 (2012) 186–198, doi:[10.1016/j.cossms.2012.05.002](https://doi.org/10.1016/j.cossms.2012.05.002).
- [2] S.B.D. Stewart, P.D. Albertus, V.D.D. Srinivasan, I. Plitz, N.D.D. Pereira, G.D.D. Amatucci, J.D.B.D. Newman, Optimizing the performance of lithium titanate spinel paired with activated carbon or iron phosphate, *J. Electrochem. Soc.* 155 (2008) A253–A261, doi:[10.1149/1.2830552](https://doi.org/10.1149/1.2830552).
- [3] Y.H. Chen, C.W. Wang, X. Zhang, A.M. Sastry, Porous cathode optimization for lithium cells: ionic and electronic conductivity, capacity, and selection of materials, *J. Power Sources* 195 (2010) 2851–2862, doi:[10.1016/j.jpowsour.2009.11.044](https://doi.org/10.1016/j.jpowsour.2009.11.044).
- [4] D. Miranda, C.M. Costa, A.M. Almeida, S. Lanceros-Méndez, Computer simulations of the influence of geometry in the performance of conventional and unconventional lithium-ion batteries, *Appl. Energy* 165 (2016) 318–328, doi:[10.1016/j.apenergy.2015.12.068](https://doi.org/10.1016/j.apenergy.2015.12.068).
- [5] S.L. Mitchell, M. Ortiz, Computational multiobjective topology optimization of silicon anode structures for lithium-ion batteries, *J. Power Sources* 326 (2016) 242–251, doi:[10.1016/j.jpowsour.2016.06.136](https://doi.org/10.1016/j.jpowsour.2016.06.136).
- [6] Y. Ji, Y. Zhang, C.-Y. Wang, Li-ion cell operation at low temperatures, *J. Electrochem. Soc.* 160 (2013) A636–A649, doi:[10.1149/2.047304jes](https://doi.org/10.1149/2.047304jes).
- [7] V. Ramadesigan, P.W.C. Northrop, S. De, S. Santhanagopalan, R.D. Braatz, V.R. Subramanian, Modeling and simulation of lithium-ion batteries from a systems engineering perspective, *J. Electrochem. Soc.* 159 (2012) R31–R45, doi:[10.1149/2.018203jes](https://doi.org/10.1149/2.018203jes).
- [8] J. Newman, Optimization of porosity and thickness of a battery electrode by means of a reaction-zone model, *J. Electrochem. Soc.* 142 (1995) 97, doi:[10.1149/1.2043956](https://doi.org/10.1149/1.2043956).
- [9] R. Darling, J. Newman, Modeling a porous intercalation electrode with two characteristic particle sizes, *J. Electrochem. Soc.* 144 (1997) 4201–4208, doi:[10.1149/1.1838166](https://doi.org/10.1149/1.1838166).
- [10] V. Srinivasan, J. Newman, Design and optimization of a natural graphite/iron phosphate lithium-ion cell, *J. Electrochem. Soc.* 151 (2004) A1530, doi:[10.1149/1.1785013](https://doi.org/10.1149/1.1785013).
- [11] J. Christensen, V. Srinivasan, J. Newman, Optimization of lithium titanate electrodes for high-power cells, *J. Electrochem. Soc.* 153 (2006) A560, doi:[10.1149/1.2172535](https://doi.org/10.1149/1.2172535).
- [12] W. Wu, X. Xiao, X. Huang, The effect of battery design parameters on heat generation and utilization in a Li-ion cell, *Electrochim. Acta* 83 (2012) 227–240, doi:[10.1016/j.electacta.2012.07.081](https://doi.org/10.1016/j.electacta.2012.07.081).
- [13] W. Du, A. Gupta, X. Zhang, A.M. Sastry, W. Shyy, Effect of cycling rate, particle size and transport properties on lithium-ion cathode performance, *Int. J. Heat Mass Transfer* 53 (2010) 3552–3561, doi:[10.1016/j.ijheatmasstransfer.2010.04.017](https://doi.org/10.1016/j.ijheatmasstransfer.2010.04.017).
- [14] M. Singh, J. Kaiser, H. Hahn, Thick electrodes for high energy lithium ion batteries, *J. Electrochem. Soc.* 162 (2015) A1196–A1201, doi:[10.1149/2.0401507jes](https://doi.org/10.1149/2.0401507jes).
- [15] M. Doyle, J. Newman, The use of mathematical modeling in the design of lithium/polymer battery systems, *Electrochim. Acta* 40 (1995) 2191–2196, doi:[10.1016/0013-4686\(95\)00162-8](https://doi.org/10.1016/0013-4686(95)00162-8).
- [16] I.V. Thorat, T. Joshi, K. Zaghib, J.N. Harb, D.R. Wheeler, Understanding rate-limiting mechanisms in LiFePO₄ cathodes for Li-ion batteries, *J. Electrochem. Soc.* 158 (2011) A1185–A1193, doi:[10.1149/2.001111jes](https://doi.org/10.1149/2.001111jes).
- [17] X. Li, S.-Y. Choe, W.T. Joe, A reduced order electrochemical and thermal model for a pouch type lithium ion polymer battery with LiNi_xMnyCo_{1-x-y}O₂/LiFePO₄ blended cathode, *J. Power Sources* 294 (2015) 545–555, doi:[10.1016/j.jpowsour.2015.06.090](https://doi.org/10.1016/j.jpowsour.2015.06.090).
- [18] E. Hosseinzadeh, R. Genieser, D. Worwood, A. Barai, J. Marco, P. Jennings, A systematic approach for electrochemical-thermal modelling of a large format lithium-ion battery for electric vehicle application, *J. Power Sources* 382 (2018) 77–94, doi:[10.1016/j.jpowsour.2018.02.027](https://doi.org/10.1016/j.jpowsour.2018.02.027).
- [19] A. Samba, N. Omar, H. Gualous, O. Capron, P. Van Den Bossche, J. Van Mierlo, Impact of tab location on large format lithium-ion pouch cell based on fully coupled three-dimensional electrochemical-thermal modeling, *Electrochim. Acta* 147 (2014) 319–329, doi:[10.1016/j.electacta.2014.08.115](https://doi.org/10.1016/j.electacta.2014.08.115).
- [20] P. Amiribavandpour, W. Shen, D. Mu, A. Kapoor, An improved theoretical electrochemical-thermal modelling of lithium-ion battery packs in electric vehicles, *J. Power Sources* 284 (2015) 328–338, doi:[10.1016/j.jpowsour.2015.03.022](https://doi.org/10.1016/j.jpowsour.2015.03.022).

- [21] M. Xu, Z. Zhang, X. Wang, L. Jia, L. Yang, Two-dimensional electrochemical-thermal coupled modeling of cylindrical LiFePO₄ batteries, *J. Power Sources* 256 (2014) 233–243, doi:[10.1016/j.jpowsour.2014.01.070](https://doi.org/10.1016/j.jpowsour.2014.01.070).
- [22] B. Wu, V. Yufit, M. Marinescu, G.J. Offer, R.F. Martinez-Botas, N.P. Brandon, Coupled thermal-electrochemical modelling of uneven heat generation in lithium-ion battery packs, *J. Power Sources* 243 (2013) 544–554, doi:[10.1016/j.jpowsour.2013.05.164](https://doi.org/10.1016/j.jpowsour.2013.05.164).
- [23] Y.M. Chiang, B. Hellweg, *Reticulated and controlled porosity battery structures*, Massachusetts Institute of Technology, Cambridge, MA (US), 2009 Patent No. US 7,553,584 B2.
- [24] V. Ramadesigan, R.N. Methekar, F. Latinwo, R.D. Braatz, V.R. Subramanian, Optimal porosity distribution for minimized ohmic drop across a porous electrode, *J. Electrochem. Soc.* 157 (2010) A1328–A1334, doi:[10.1149/1.3495992](https://doi.org/10.1149/1.3495992).
- [25] S. Golmon, K. Maute, M.L. Dunn, A design optimization methodology for Li⁺ batteries, *J. Power Sources* 253 (2014) 239–250, doi:[10.1016/j.jpowsour.2013.12.025](https://doi.org/10.1016/j.jpowsour.2013.12.025).
- [26] L.M. Deschere, *Fuel Cell with Variable Porosity*, vol. 1, 2003.
- [27] Y. Wang, K.S. Chen, Effect of spatially-varying GDL properties and land compression on water distribution in PEM fuel cells, *J. Electrochem. Soc.* 158 (2011) B1292, doi:[10.1149/2.015111jes](https://doi.org/10.1149/2.015111jes).
- [28] N.P. Brandon, D.J. Brett, Engineering porous materials for fuel cell applications, *Philos. Trans. R. Soc. A* 364 (2006) 147–159, doi:[10.1098/rsta.2005.1684](https://doi.org/10.1098/rsta.2005.1684).
- [29] K. Smith, C.-Y. Wang, Power and thermal characterization of a lithium-ion battery pack for hybrid-electric vehicles, *J. Power Sources* 160 (2006) 662–673, doi:[10.1016/j.jpowsour.2006.01.038](https://doi.org/10.1016/j.jpowsour.2006.01.038).
- [30] J. Song, M.Z. Bazant, Effects of nanoparticle geometry and size distribution on diffusion impedance of battery electrodes, *J. Electrochem. Soc.* 160 (2013) A15–A24, doi:[10.1149/2.023301jes](https://doi.org/10.1149/2.023301jes).
- [31] G.B. Less, J.H. Seo, S. Han, A.M. Sastry, J. Zausch, A. Latz, S. Schmidt, C. Wieser, D. Kehrwald, S. Fell, Micro-scale modeling of Li-ion batteries: parameterization and validation, *J. Electrochem. Soc.* 159 (2012) A697, doi:[10.1149/2.096205jes](https://doi.org/10.1149/2.096205jes).
- [32] M. Doyle, T.P. Fuller, J. Newman, Modeling of galvanostatic charge and discharge of the lithium/polymer/insertion cell, *J. Electrochem. Soc.* 139 (1992) 79–96.
- [33] R.W. Zimmerman, D.-W. Chen, N.G.W. Cook, Lawrence Berkeley Laboratory, *J. Hydrology* 139 (1992) 79–96, doi:[10.1149/1.2221597](https://doi.org/10.1149/1.2221597).
- [34] M. Jabbari, V.A. Jambekar, J.H. Hattel, R. Helmig, Drying of a tape-cast layer: numerical modelling of the evaporation process in a graded/layered material, *Int. J. Heat Mass Transfer* 103 (2016) 1144–1154, doi:[10.1016/j.jheatmasstransfer.2016.08.073](https://doi.org/10.1016/j.jheatmasstransfer.2016.08.073).
- [35] A. Vadakkepatt, B. Trembacki, S.R. Mathur, J.Y. Murthy, Bruggeman's exponents for effective thermal conductivity of lithium-ion battery electrodes, *J. Electrochem. Soc.* 163 (2016) A119–A130, doi:[10.1149/2.0151602jes](https://doi.org/10.1149/2.0151602jes).
- [36] G. Sikha, B.N. Popov, R.E. White, Effect of porosity on the capacity fade of a lithium-ion battery, *J. Electrochem. Soc.* 151 (2004) A1104, doi:[10.1149/1.1759972](https://doi.org/10.1149/1.1759972).
- [37] I.V. Thorat, D.E. Stephenson, N.A. Zacharias, K. Zaghib, J.N. Harb, D.R. Wheeler, Quantifying tortuosity in porous Li-ion battery materials, *J. Power Sources* 188 (2009) 592–600, doi:[10.1016/j.jpowsour.2008.12.032](https://doi.org/10.1016/j.jpowsour.2008.12.032).
- [38] J. Li, Y. Cheng, L. Ai, M. Jia, S. Du, B. Yin, S. Woo, H. Zhang, 3D simulation on the internal distributed properties of lithium-ion battery with planar tabbed configuration, *J. Power Sources* 293 (2015) 993–1005, doi:[10.1016/j.jpowsour.2015.06.034](https://doi.org/10.1016/j.jpowsour.2015.06.034).
- [39] J. Li, Y. Cheng, M. Jia, Y. Tang, Y. Lin, Z. Zhang, Y. Liu, An electrochemical-thermal model based on dynamic responses for lithium iron phosphate battery, *J. Power Sources* 255 (2014) 130–143, doi:[10.1016/j.jpowsour.2014.01.007](https://doi.org/10.1016/j.jpowsour.2014.01.007).
- [40] E. Hosseinzadeh, J. Marco, P. Jennings, Electrochemical-thermal modelling and optimisation of lithium-ion battery design parameters using analysis of variance, *Energies* 10 (2017) 1278, doi:[10.3390/en10091278](https://doi.org/10.3390/en10091278).
- [41] B. Suthar, P.W.C. Northrop, D. Rife, V.R. Subramanian, Effect of porosity, thickness and tortuosity on capacity fade of anode, *J. Electrochem. Soc.* 162 (2015) A1708–A1717, doi:[10.1149/2.0061509jes](https://doi.org/10.1149/2.0061509jes).
- [42] D.M. Bernardi, J.Y. Go, Analysis of pulse and relaxation behavior in lithium-ion batteries, *J. Power Sources* 196 (2011) 412–427, doi:[10.1016/j.jpowsour.2010.06.107](https://doi.org/10.1016/j.jpowsour.2010.06.107).
- [43] F. Jiang, P. Peng, Y. Sun, Thermal analyses of LiFePO₄/graphite battery discharge processes, *J. Power Sources* 243 (2013) 181–194, doi:[10.1016/j.jpowsour.2013.05.089](https://doi.org/10.1016/j.jpowsour.2013.05.089).
- [44] C. Huang, N.P. Young, J. Zhang, H.J. Snaith, P.S. Grant, A two layer electrode structure for improved Li ion diffusion and volumetric capacity in Li ion batteries, *Nano Energy* 31 (2016) 377–385, doi:[10.1016/j.nanoen.2016.11.043](https://doi.org/10.1016/j.nanoen.2016.11.043).